



● Original Contribution

SOURCES OF VARIABILITY IN SHEAR WAVE SPEED AND DISPERSION QUANTIFICATION WITH ULTRASOUND ELASTOGRAPHY: A PHANTOM STUDY

NAIARA KORTA MARTIARTU, SHERIN NAMBIAR, IARA NASCIMENTO KIRCHNER, CATHERINE PAVERD, DAVIDE CESTER, THOMAS FRAUENFELDER, LISA RUBY, and MARGA B. ROMINGER
 Institute of Diagnostic and Interventional Radiology, University Hospital Zurich, Rämistrasse 100, 8091 Zürich, Switzerland

(Received 14 May 2021; revised 2 August 2021; in final form 14 August 2021)

Abstract—There is a growing interest in quantifying shear-wave dispersion (SWD) with ultrasound shear-wave elastography (SWE). Recent studies suggest that SWD complements shear-wave speed (SWS) in diffuse liver disease diagnosis. To accurately interpret these metrics in clinical practice, we analyzed the impact of operator-dependent acquisition parameters on SWD and SWS measurements. Considered parameters were the acquisition depth, lateral position and size of the region of interest (ROI), as well as the size of the SWE acquisition box. Measurements were performed using the Canon Aplio i800 system (Canon Medical Systems, Otawara, Tochigi, Japan) and four homogeneous elasticity phantoms with certified stiffness values ranging from 3.7 to 44 kPa. In general, SWD exhibited two to three times greater variability than SWS. The acquisition depth was the main variance-contributing factor for both SWS and SWD, which decayed significantly with depth. The lateral ROI position contributed as much as the acquisition depth to the total variance in SWD. Locations close to the initial shear-wave excitation pulse were more robust to biases because of inaccurate probe–phantom coupling. The size of the ROI and acquisition box did not introduce significant variations. These results suggest that future guidelines on multiparametric elastography should account for the depth- and lateral-dependent variability of measurements. (E-mail: naiara.kortamartiartu@usz.ch) © 2021 The Author(s). Published by Elsevier Inc. on behalf of World Federation for Ultrasound in Medicine & Biology. This is an open access article under the CC BY-NC-ND license (<http://creativecommons.org/licenses/by-nc-nd/4.0/>).

Key Words: Ultrasound, Shear wave elastography, Shear wave speed, Shear wave dispersion, Liver, Diffuse liver disease, Liver fibrosis, Liver cirrhosis, Phantom, Variability.

INTRODUCTION

Chronic liver disease involves a wide spectrum of etiologies including alcohol-related liver damage, non-alcoholic fatty liver disease and chronic viral infections (Wiegand and Berg 2013). It is characterized by progressive hepatic fibrosis, which may ultimately develop into cirrhosis, a major cause of death worldwide with approximately 1 million deaths per year (Asrani et al. 2019). Accurate diagnosis of the stage of liver fibrosis is essential for monitoring disease progression and evaluating treatment strategies and prognosis. Liver biopsy has traditionally been the reference standard for fibrosis staging. However, it is an invasive technique limited by sampling, inter-observer and intra-observer variability (Regev et al. 2002;

Bedossa et al. 2003; Rousselet et al. 2005). These limitations have stimulated the development of non-invasive methods to assess liver fibrosis (Castera 2012, 2015)

Shear-wave elastography (SWE) is a commercially available ultrasound (US) modality that shows great promise for non-invasive liver fibrosis staging (Shiina et al. 2015; Ferraioli et al. 2018). In SWE, an acoustic radiation force, namely, a focused US beam, is used to deform internal tissue and generate laterally propagating shear waves. By measurement of the propagation velocity of shear waves, this technology provides real-time 2-D maps of shear-wave speed (SWS) superimposed on B-mode images. SWS is directly related to tissue stiffness, which has proven to be particularly useful in identifying patients with moderate to severe fibrosis (stages II–IV) or cirrhosis (stage IV) (Talwalkar et al. 2007).

In SWE, tissue is assumed to be a purely elastic medium to quantify tissue stiffness from SWS measurements. However, all biological tissues are inherently

Address correspondence to: Naiara Korta Martiartu, Zurich Ultrasound Research and Translation (ZURT), Institute of Diagnostic and Interventional Radiology, University Hospital Zurich, Rämistrasse 100, 8091 Zürich, Switzerland. E-mail: naiara.kortamartiartu@usz.ch

viscoelastic, and such simplifications may confound SWS measurements. Biases introduced by inaccurate physical models have been extensively studied in the literature (Zhao et al. 2011; Chang et al. 2013; Shin et al. 2016; Ruby et al. 2019). For instance, it is well known that SWS values gradually decrease with increasing acquisition depth (Tozaki et al. 2011; Zhao et al. 2011; Hall et al. 2013; Ewertsen et al. 2016; Shin et al. 2016; Ruby et al. 2019). This behavior is attributed to the shear-wave dispersion (SWD), that is, the frequency dependence of shear waves in viscous media (Tozaki et al. 2011; Carlsen et al. 2015; Ruby et al. 2019). The quantification of SWD is therefore useful to capture the complexity of the shear-wave propagation in tissue, as well as to characterize tissue viscosity. Moreover, SWD is expected to have diagnostic value complementary to that of SWS. A recent animal study revealed that SWD was significantly related to the degree of liver necro-inflammation, while SWS correlated with fibrosis stages (Sugimoto et al. 2018). The same authors also extended their analysis to patients with biopsy-proven non-alcoholic fatty liver disease reporting similar findings (Sugimoto et al. 2020).

Currently, SWD quantification is emerging in commercial US scanners (Chen et al. 2013; Nguyen et al. 2014; Sugimoto et al. 2018, 2019; Lee et al. 2019; Trout et al. 2020). Before its application in clinical practice, it is essential to develop a good understanding of the acquisition parameters that may influence the reliability of SWD measurements. The goal of our study was to analyze the sensitivity of SWS and SWD measurements to changes in acquisition parameters that are subject to operator choice. These parameters included the acquisition depth, the size and location of the region of interest (ROI) and the size of the SWE acquisition box. The variability arising from the examined medium was controlled using homogeneous elasticity phantoms.

METHODS

Study design

This study analyzed the variability of SWS and SWD measurements using four elasticity phantoms. During measurements, the US probe was fixed in a stationary position using a clamp (Fig. 1). This was useful to minimize unwanted sources of variability arising from operator-dependent motion and US probe pressure. The confounding variables studied were the lateral position, acquisition depth, size of the circular ROI and size of the acquisition box in which the SWE was performed (Figs. 2 and 3). All measurements were performed by two operators with specific training provided by the manufacturer of the US system.

Phantoms

This study used four certified homogeneous isotropic elasticity phantoms (Shear Wave Liver Fibrosis Phantom, Model 039, Computerized Imaging Reference

Systems, Inc. [CIRS], Norfolk, VA, USA) (Fig. 1). These phantoms have the same elastic properties in every location (homogeneous) and wave propagation direction (isotropic). All phantoms are filled with Zerdine solid elastic hydrogel, are cylindrical and are 10 cm in diameter and 12 cm high. Certified properties of the phantoms are summarized in Table 1. The stiffness of the phantoms covers the range of normal and cirrhotic liver, with elasticity values of 3.7 kPa (phantom P1), 12 kPa (P2), 25 kPa (P3) and 44 kPa (P4). The manufacturer reported uncertainties in elasticity measurements with a standard deviation of 5% and a phantom density of $\rho = 1030 \text{ kg/m}^3$. Table 1 also lists the corresponding SWS velocities. We computed these from reported values of the Young's modulus (E) following the equivalence $E = 3\rho\text{SWS}^2$, which holds for incompressible materials (Shiina et al. 2015). These phantoms do not have certified values of SWD. Because the phantoms have homogeneous elasticity properties, we make the same assumption for SWD values. That is, we assume that all locations of the phantom have the same value of SWD. To be consistent with certified phantom properties, all measurements were done at room temperature.

Shear-wave elastography

Two-dimensional SWE examinations were performed using the Canon Aplio i800 US system (Canon Medical Systems Corp., Otawara, Tochigi, Japan) and the i8CX1 convex US probe, which has a center frequency of 4 MHz. The system displays a color-coded map of the spatial distribution of elasticity values (acquisition box) superimposed on the B-mode image (e.g., Fig. 2a). It also displays a propagation map revealing shear-wave arrival time contours (Fig. 2a). The two maps are viewed simultaneously, and the propagation map serves as quality control. The measurement protocol of the manufacturer recommends placing a 10-mm-diameter ROI in the area with the most parallel propagation contours (Lee et al. 2019), preferably in the upper part of the acquisition box (Fig. 2a). In homogeneous phantoms, this condition is usually satisfied in the upper left corner of the acquisition box. This is the region in which the first excitation pulse for generating shear waves (push pulse) is located. The push pulse generates an acoustic radiation force strong enough to deform the tissue and generate shear waves. Tissue displacement is measured at each location as a function of time and Fourier transformed to the frequency domain. From these data, shear-wave phase velocities are computed from the phase differences between two measurement locations at the same depth (Sugimoto et al. 2018, 2019; Lee et al. 2019, 2021). The phase velocities assessed correspond to frequencies approximately in the range of 50–300 Hz (Nightingale et al. 2015; Lipman et al. 2018;

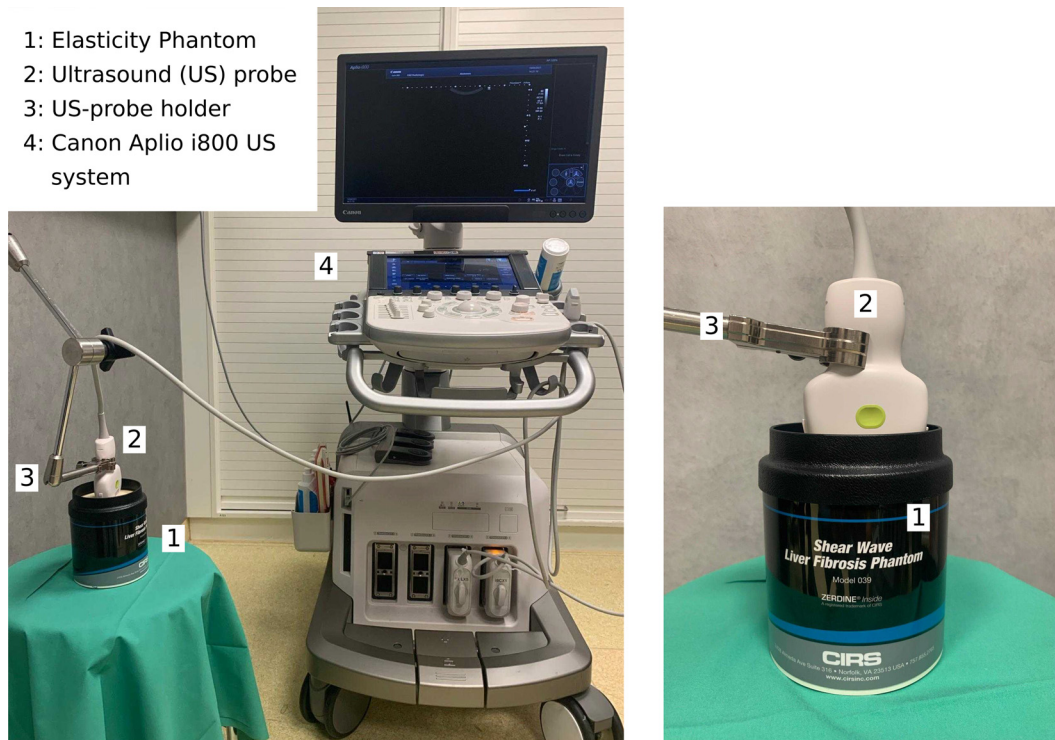


Fig. 1. Experimental setup. (1) Four certified isotropic elasticity phantoms were used for the study (CIRS, Model 039, Shear Wave Liver Fibrosis). (2, 3) The ultrasound (US) probe was placed on top of the phantom and fixed with a mechanical clamp (US-probe holder). (4) Shear wave speed and dispersion measurements were acquired using the Canon Aplio i800 US system.

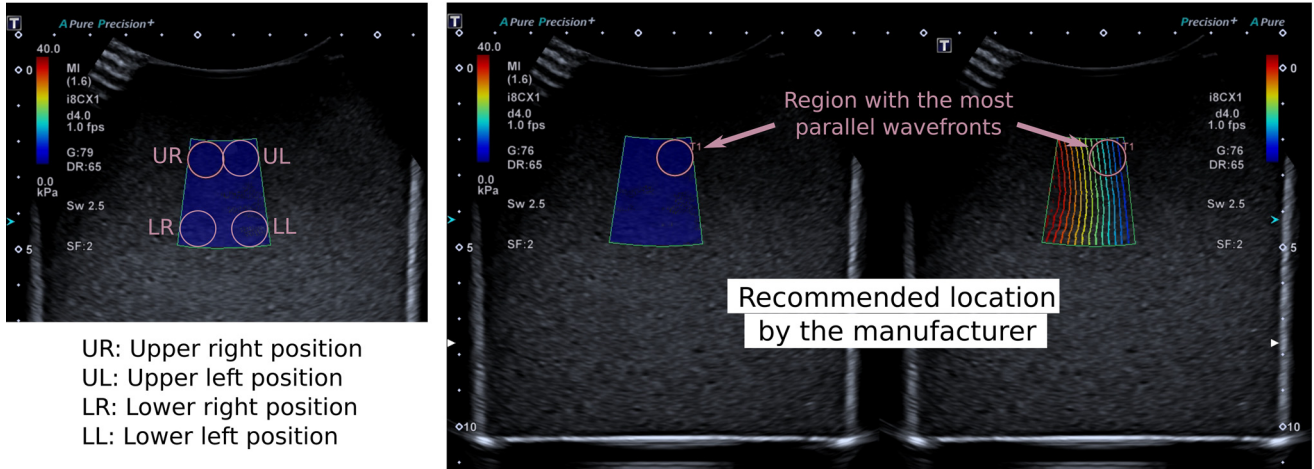
Ormachea and Parker 2020). The US system computes the slope of the SWD curve to provide a single metric related to shear-wave dispersion. In this article, we refer to this slope metric as SWD (Sugimoto *et al.* 2019). Following this computation, the US system displays the average SWS (in m/s) and SWD (in m/s/kHz) within the ROI together with their standard deviations. In this study, SWS and SWD measurements were repeated 10 times in every location, and the values were used for the statistical analyses.

Experimental procedure: Confounder analysis

Three types of measurements were performed to assess the variability caused by (i) the ROI position within the acquisition box, (ii) the acquisition depth of the ROI and (iii) the size of the ROI. The first group of measurements was collected using a standard ROI size (10 mm diameter) and fixing the upper part of the acquisition box at 20 mm below the US probe. As illustrated in Figure 2a, the ROI was placed in four different positions within the acquisition box: upper left corner (UL), upper right corner (UR), lower left corner (LL) and lower right corner (LR). These measurements allowed us to analyze the lateral variability by comparing values at right and left positions.

The second group of measurements was collected using a standard ROI size in the UL position and moving the acquisition box to different depths. In this way, the center of the ROI was positioned at depths of 25, 45 and 65 mm (Fig. 2b). These values cover the range of depths relevant to liver assessment, consistent with similar studies analyzing depth-dependent biases (Chang *et al.* 2013; Hall *et al.* 2013; Wang *et al.* 2014; Dhyani *et al.* 2018; Palmeri *et al.* 2021). For the third group of measurements, the acquisition box was fixed at 20 mm below the US probe, and the ROI was placed in the center of the box. The size of the ROI was increased in steps of 5 mm, ranging from a diameter of 5 mm to a size encompassing the whole acquisition box (Fig. 3a). Furthermore, the variability caused by the size of the acquisition box was assessed by repeating all types of measurements using different acquisition box sizes. Three sizes were considered with dimensions 15 × 15 mm (small box), 20 × 30 mm (medium box, standard) and 40 × 35 mm (large box) (Fig. 3b). To avoid data inconsistencies, all SWS and SWD measurements were acquired without unmounting the US probe from the holder. The probe was displaced only when the entire procedure was completed for each

(a) Varying ROI position within the acquisition box



(b) Varying acquisition depth

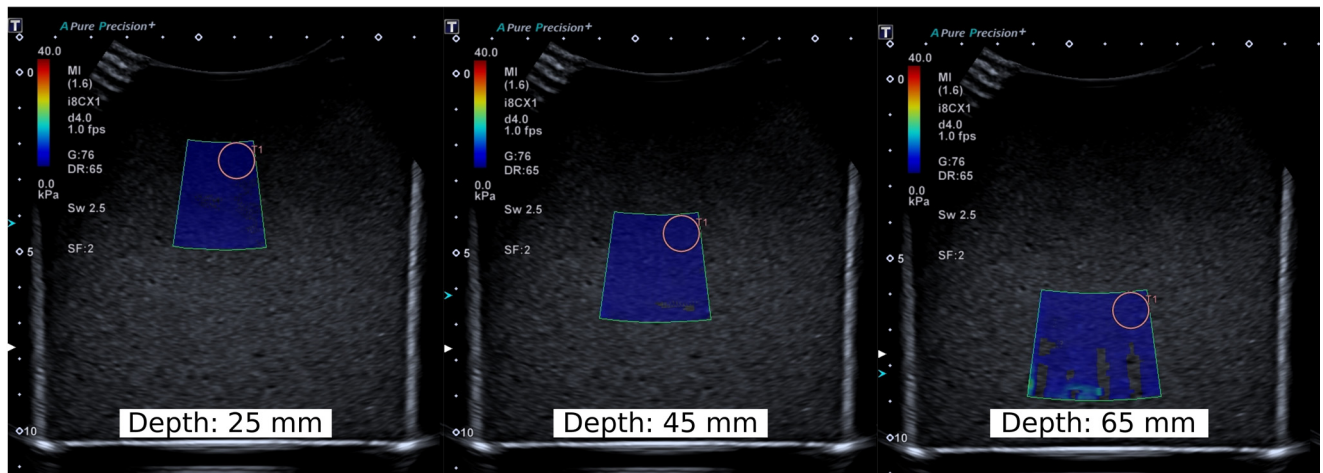


Fig. 2. Experimental procedure for analyzing confounding variables. (a) The variability caused by the region of interest (ROI) position was studied by comparing measurements in four different locations within the acquisition box. The manufacturer recommends placing the ROI in the area with the most parallel wavefronts, preferably in the upper part of the acquisition box (rightmost image). In homogeneous phantoms, this is the upper left corner of the acquisition box. (b) The measurement variability with acquisition depth was assessed by placing the ROI at depths of 25, 45 and 65 mm. All measurements were acquired using the standard ROI size (10-mm diameter).

phantom. In total, we acquired 1752 measurements for both SWS and SWD.

Validation experiment: Lateral variability

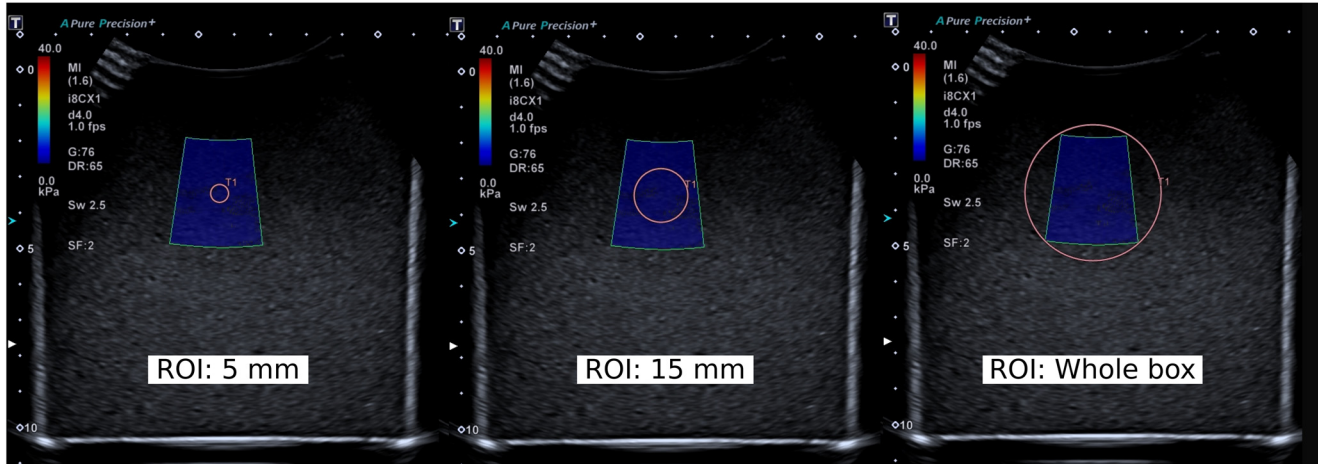
Additional measurements were performed to understand the variability caused by the lateral ROI position. We compared SWS and SWD values in UL and UR positions, gradually modifying the coupling conditions between the US probe, gel and phantom. Ten different conditions were considered that ranged from perfect coupling with generous gel quantity to poor coupling on one or both sides of the probe. The coupling conditions were controlled with the help of B-mode images. For instance, reverberation and acoustic shadowing artifacts in B-

mode images indicate inadequate probe–phantom coupling (e.g., artifacts in the upper left part of the images in Fig. 2). The measurements were performed using phantom P2 and standard sizes for the ROI and acquisition box. SWS and SWD measurements were provided simultaneously by the US system. Therefore, both metrics were measured under identical coupling conditions. In total, 200 measurements were acquired for both SWS and SWD.

Statistical analysis

Statistical analysis and visualization were performed using Python (Version 3.7.9) with the SciPy (1.6.0), Pandas (1.2.1), Seaborn (0.11.1) and Scikit-learn

(a) Varying size of the region of interest



(b) Varying size of the acquisition box

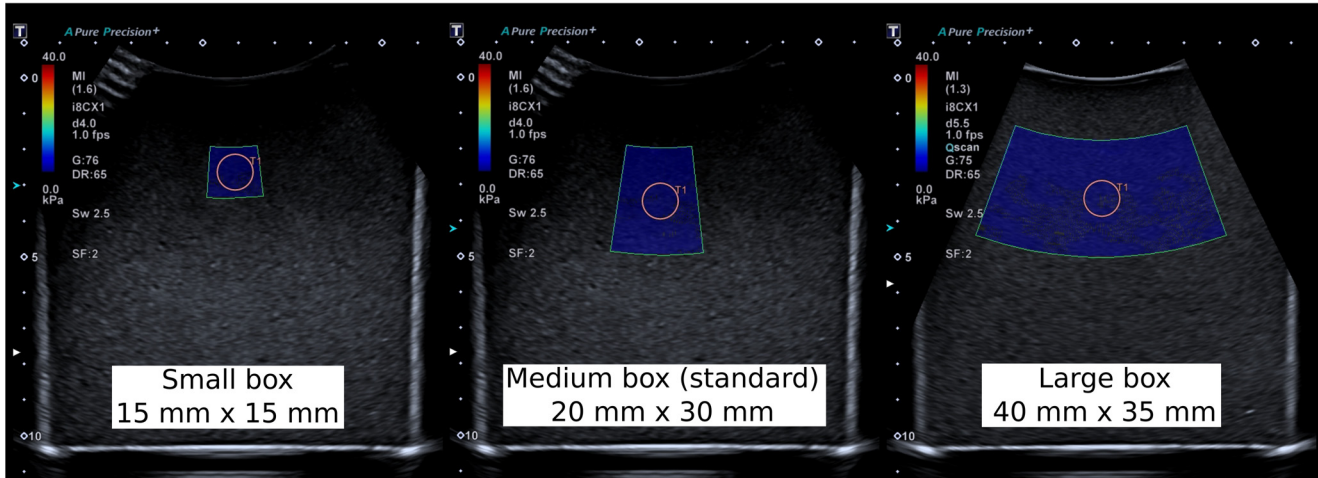


Fig. 3. Experimental procedure for analyzing confounding variables. (a) The measurement variability caused by the size of the region of interest (ROI) was assessed by comparing five different ROI sizes with diameters of 5, 10, 15 and 20 mm and a size encompassing the whole acquisition box. The ROI was located at the mid-center position of the acquisition box. (b) Three different acquisition box sizes were considered for the analysis. Dimensions are indicated as width \times height. The acquisition box is the region in which 2-D shear wave elastography is performed.

(0.24.1) libraries. D'Agostino's K^2 test was used to verify that the data follow a Gaussian distribution. White's Lagrange multiplier test was applied to test for hetero-

Table 1. Mechanical properties of the phantoms given by the manufacturer

Phantom	Young's modulus, E (kPa)	Shear wave speed (m/s)	Speed of sound (m/s)	Attenuation (dB/cm/MHz)
P1	3.7 [± 0.2]*	1.09 [± 0.03]	1531	0.47
P2	12 [± 0.6]	1.97 [± 0.05]	1532	0.49
P3	25 [± 1.3]	2.84 [± 0.07]	1535	0.51
P4	44 [± 2.2]	3.77 [± 0.09]	1534	0.51

* The brackets specify the standard deviations provided by the manufacturer.

scedasticity. Measurements were described in terms of mean, standard deviation and coefficient of variation (CoV). The latter describes the measurement variability. For non-Gaussian distributions, the variability was given by the ratio between the interquartile range and the median. A machine-learning algorithm known as random forest regression (Breiman 2001) was used to model the relationship between SWS and SWD measurements and confounding variables. This algorithm allowed us to model complex interactions between confounding variables and SWS/SWD, which is useful to understand the importance of each confounder in the variability of SWS and SWD. The importance was estimated using the feature permutation method (Breiman 2001). This method quantifies the reduction in the model accuracy (R^2)

when confounding variables are randomly reshuffled. In addition, multivariate robust log-linear regression was used to analyze the significance of linear trends in the data with respect to confounding variables. Robust log-linear models were chosen because of data heteroscedasticity. p values <0.05 were considered to indicate statistical significance. Statistical differences between measurements were analyzed with the paired sample t -test (mean), F -test (variance) and Mood's test (median). In cases with significantly different variances, Welch's t -test was used to analyze differences in the mean.

RESULTS

Descriptive analysis

SWS and SWD measurements were normally distributed for each phantom ($p < 0.001$). Figure 4 illustrates their distribution as boxplots, displaying the median and interquartile ranges. Here, we also indicate the certified SWS values in red. Overall, we found an underestimation of SWS for all phantoms. Table 2 lists the mean, standard deviation and CoV for both metrics. Differences in the means of SWS and SWD were significant for all phantoms ($p < 0.001$). The measurement variability was considerably larger for SWD than for SWS and increased with phantom stiffness (heteroscedasticity $p < 0.001$).

Confounder importance

The accuracy of the random forest regression model was 0.99 for SWS and 0.92 for SWD. These values were

Table 2. Means and standard deviations of shear wave speed and dispersion when all measurements are aggregated.

Phantom	Shear-wave speed (m/s)	Shear-wave dispersion (m/s/kHz)
P1	0.83 ± 0.05 [6.1%]*	7.05 ± 1.28 [18.2%]
P2	1.47 ± 0.05 [3.7%]	10.38 ± 0.71 [6.8%]
P3	2.46 ± 0.16 [6.7%]	18.65 ± 3.62 [19.4%]
P4	3.57 ± 0.62 [17.3%]	26.07 ± 8.29 [31.8%]

* The variability of the data is given by the coefficient of variation (in brackets).

computed in a subsample of the data that was not used for training the model. Figure 5 illustrates the importance of each confounding variable to the outcome of the model. In essence, the figure indicates what portion of the total variance is attributed to each confounder. As expected, the stiffness of the phantom introduced the largest variability in SWS and SWD. The relative variability caused by other confounders was larger for SWD than for SWS. The second most important factor was the acquisition depth of the measurements. For SWD, the lateral position of the ROI was as important as its acquisition depth but had negligible effects on SWS. The size of the ROI and acquisition box had the smallest confounding effects on the data.

Variability with the ROI location

We measured SWS and SWD placing the ROI at different locations inside the acquisition box (Figure 2a). The CoV values with all measurements aggregated were 3.7% (P1), 4.1% (P2), 5.3% (P3) and 10.1% (P4) for

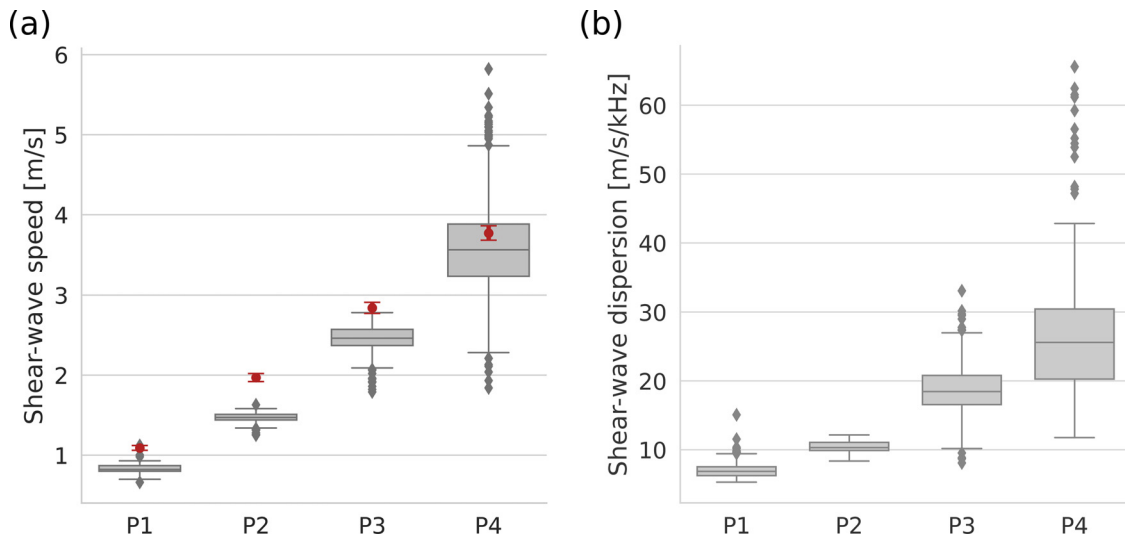


Fig. 4. Boxplots representing the distribution of (a) shear-wave speed and (b) dispersion measurements for each phantom (P1–P4). Red dots in (a) indicate the certified shear-wave speed values with error bars according to reported standard deviations. A general underestimation of speed values is observed. Mean differences between phantoms are significant for both metrics ($p < 0.001$).

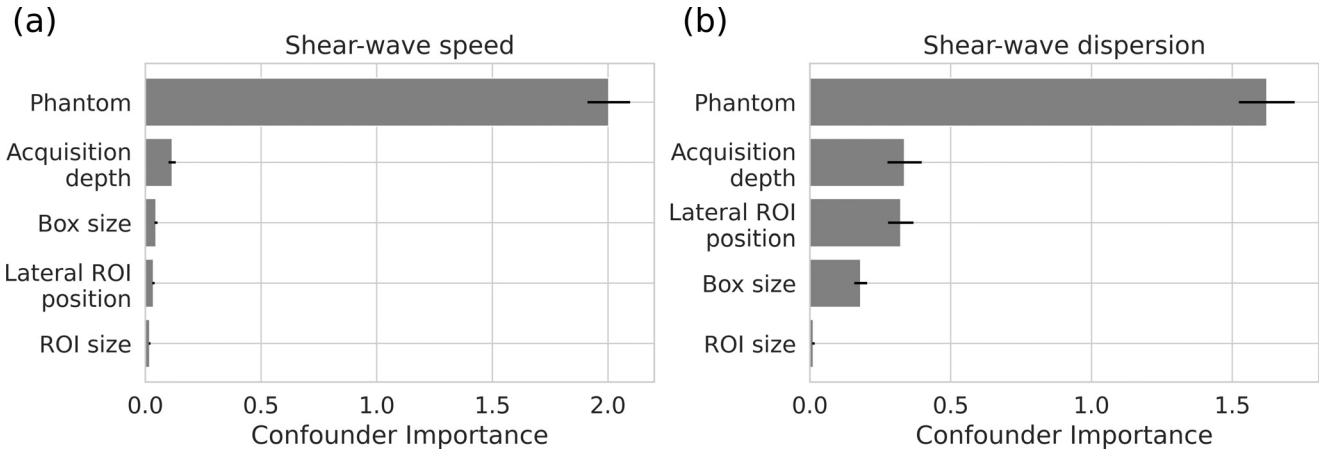


Fig. 5. Confounding variable importance for (a) shear wave velocity and (b) dispersion measurements. The importance indicates the decrease in random forest model accuracy when the values of each confounder are randomly shuffled. Error bars represent standard deviations computed from different permutations. The confounder variable “Phantom” refers to viscoelastic phantom properties. ROI = region of interest.

SWS and 20.0% (P1), 4.1% (P2), 23.8% (P3) and 25.1% (P4) for SWD. Figure 6 illustrates the values of SWS and SWD for each ROI location. Overall, we found significant differences between positions in both metrics. SWS varied more significantly because of changes in acquisition depth (UL/UR–LL/LR) than changes in lateral ROI position (UL–UR, LL–LR). In contrast, SWD had higher sensitivity to the lateral ROI position. Here, changes between left and right positions were significant for all phantoms and for both upper and lower regions. SWD values were higher in locations on the left than on the right. These changes became stronger with increasing stiffness of the phantom. To understand the overall significance of this effect, we performed a robust log-linear regression analysis taking all the acquired data into account. The results indicated that SWD significantly decreased ($p = 0.001$) from left to right positions. There was also a small but significant ($p < 0.01$) decrease in SWS.

Variability with the acquisition depth

We measured SWS and SWD values at three acquisition depths (25, 45 and 65 mm) using the standard ROI and acquisition box size (Fig. 2b). The CoV values with all depths aggregated were 2.3% (P1), 2.2% (P2), 7.4% (P3) and 8.5% (P4) for SWS and 22.2% (P1), 8.6% (P2), 23.6% (P3) and 23.2% (P4) for SWD. Variability in SWS caused by acquisition depth increased with phantom stiffness. Variability in SWD was similar for P1, P3 and P4 and higher than variability in SWS. Phantom P2 exhibited substantially less variability (8.6%). Figure 7 illustrates SWS and SWD values as a function of acquisition depth. Overall, SWS and SWD values tended to decrease with acquisition depth. The decay was more pronounced with increasing stiffness. However, the

softest phantom exhibited a significant increasing trend with depth for SWD. The robust log-linear regression analysis with all the data revealed that the decay of SWS was significant ($p < 0.001$). In contrast, SWD exhibited a small but significant increase ($p = 0.001$). This was caused by the dominant effect of the softest phantom (P1), in which SWD increased significantly with depth ($p < 0.001$). When the data from this phantom were excluded, SWD was found to have a significant decrease ($p < 0.001$).

Variability with ROI size

We measured SWS and SWD using circular ROIs with different diameters and a fixed acquisition depth at 35 mm (Fig. 3a). The CoV values with all sizes aggregated were 1.6% (P1), 1.5% (P2), 2.0% (P3) and 14.7% (P4) for SWS and 1.8% (P1), 3.6% (P2), 13.4% (P3) and 23.3% (P4) for SWD. The variability caused by ROI size was in general lower than the variability caused by changes in acquisition depth and lateral position of the ROI. Figure 8 illustrates SWS and SWD values for each ROI size and phantom. Increasing the ROI size reduced measurement variability. The absolute reduction in CoV from the smallest to the largest ROI was approximately 7% for SWS and 20% for SWD. The robust log-linear regression analysis did not reveal any significant relationship between the two metrics and ROI size.

Variability with the acquisition box

We analyzed the variability of SWS and SWD caused by the size of the acquisition box (Fig. 3b). The CoV values with all sizes aggregated were 1.6% (P1), 2.2% (P2), 2.5% (P3) and 6.5% (P4) for SWS and 5.7% (P1), 6.8% (P2), 18.4% (P3) and 14.2% (P4) for SWD.

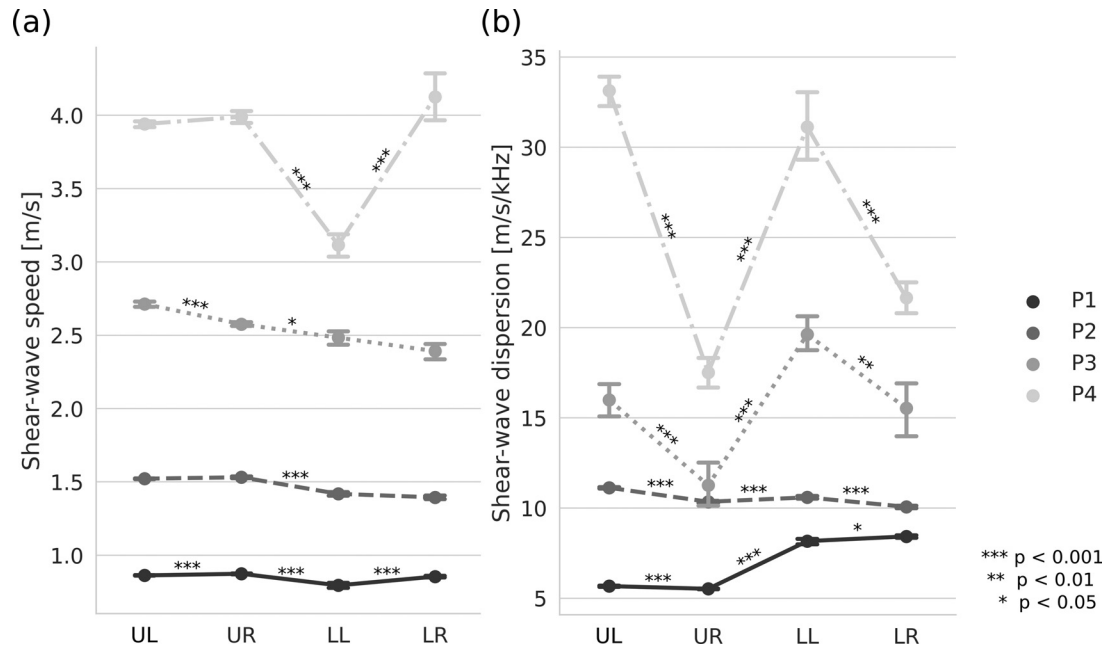


Fig. 6. (a) Shear-wave speed and (b) shear-wave dispersion as a function of the region-of-interest location in the acquisition box. Values are indicated using the mean and 95% confidence interval. Figures give the statistical significance in mean differences between consecutive pairs of values. Phantom (P) elasticity is indicated by color with increasing stiffness from P1 to P4. UL = upper left; UR = upper right; LL = lower left; LR = lower right.

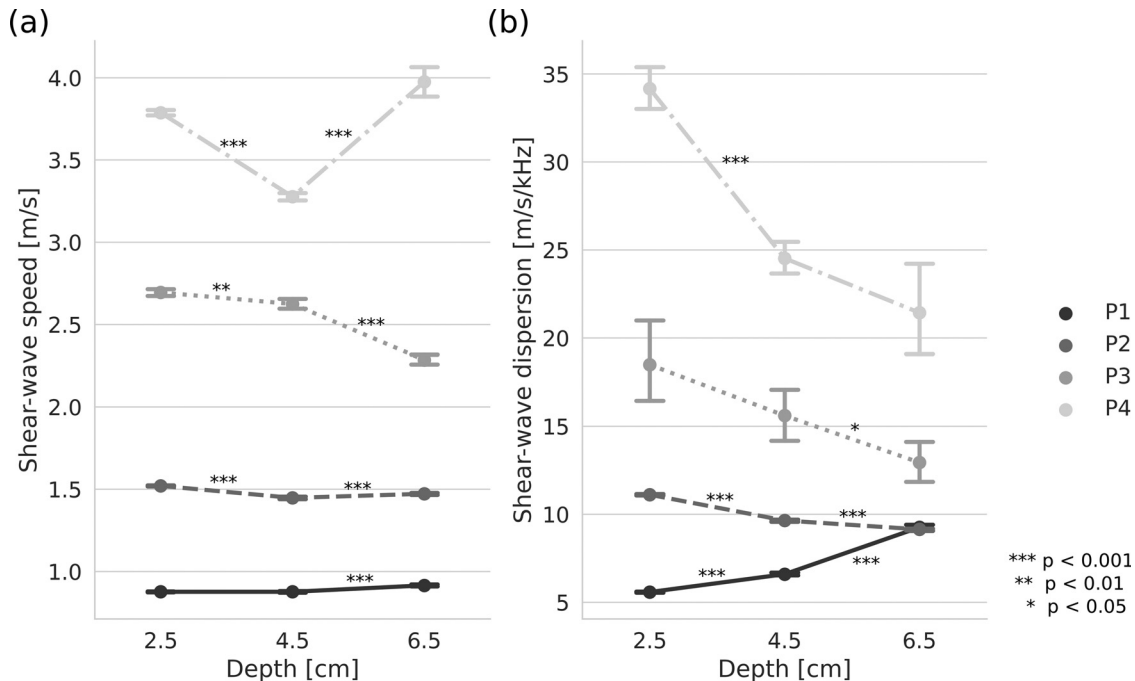


Fig. 7. (a) Shear-wave speed and (b) shear-wave dispersion as a function of the acquisition depth and viscoelastic phantom properties (P1–P4).

Figure 9 illustrates the specific variations within each phantom. The variability caused by the size of the acquisition box was comparable to that observed with varying ROI size. In all phantoms, the largest box had the largest

variability in both SWS and SWD. The robust log-linear regression analysis did not show reveal significant relationship between the two metrics and the size of the acquisition box.

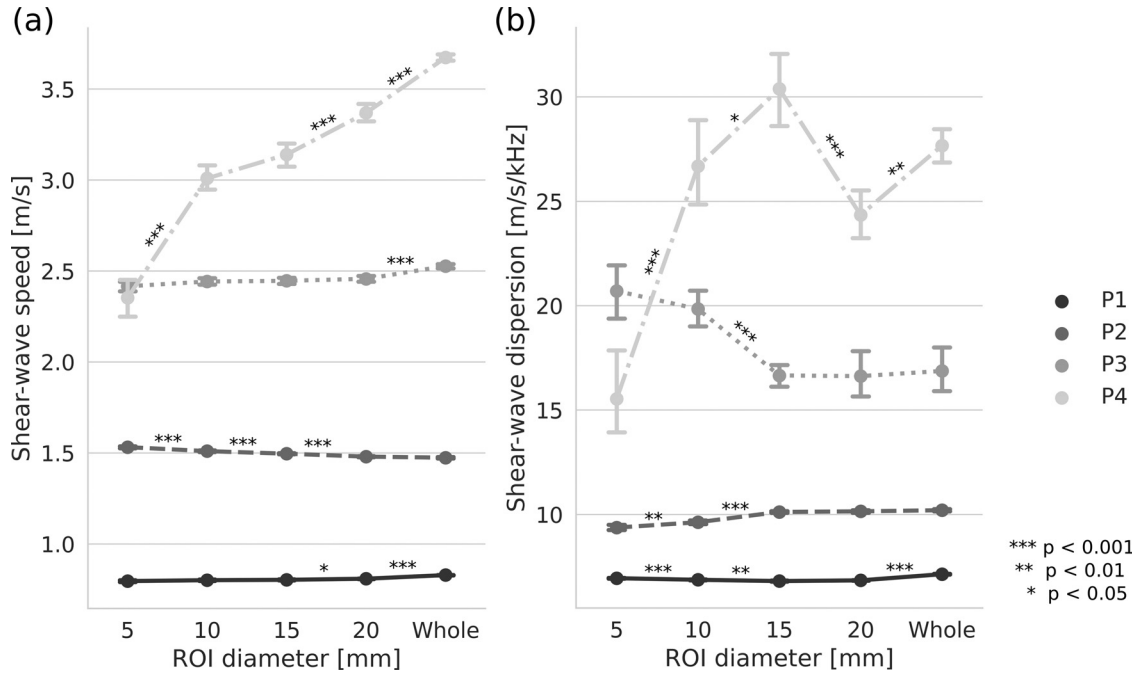


Fig. 8. (a) Shear-wave speed and (b) shear-wave dispersion as a function of the region-of-interest (ROI) size and viscoelastic phantom properties (P1–P4). The size “Whole” refers to an ROI size that encompasses the whole acquisition box.

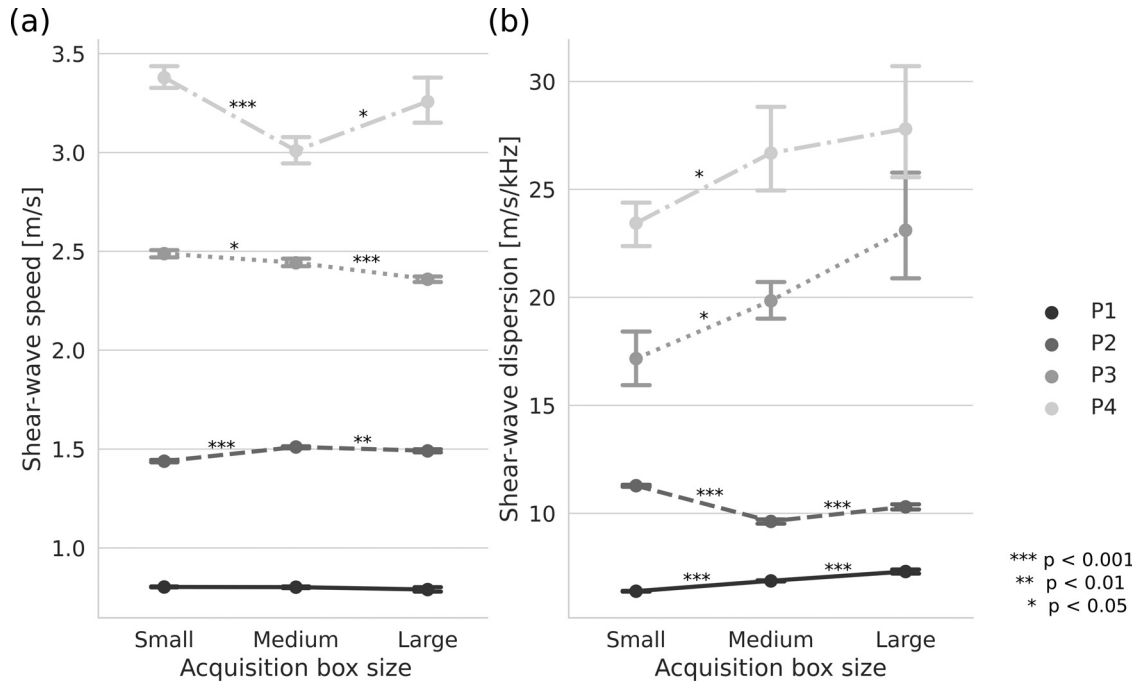


Fig. 9. (a) Shear-wave speed and (b) shear-wave dispersion for different acquisition box sizes and viscoelastic phantom properties (P1–P4). The dimensions of different acquisition boxes are indicated in Figure 3b.

Probe–phantom coupling effects on lateral variability

We analyzed the influence of different probe–phantom coupling conditions on the variability caused by the lateral ROI position. Figure 10 compares the

SWS and SWD values measured at UL and UR positions of the acquisition box (Fig. 2a) with all conditions aggregated. SWD had larger variability than SWS, especially for the UR position. In particular, SWD measurements

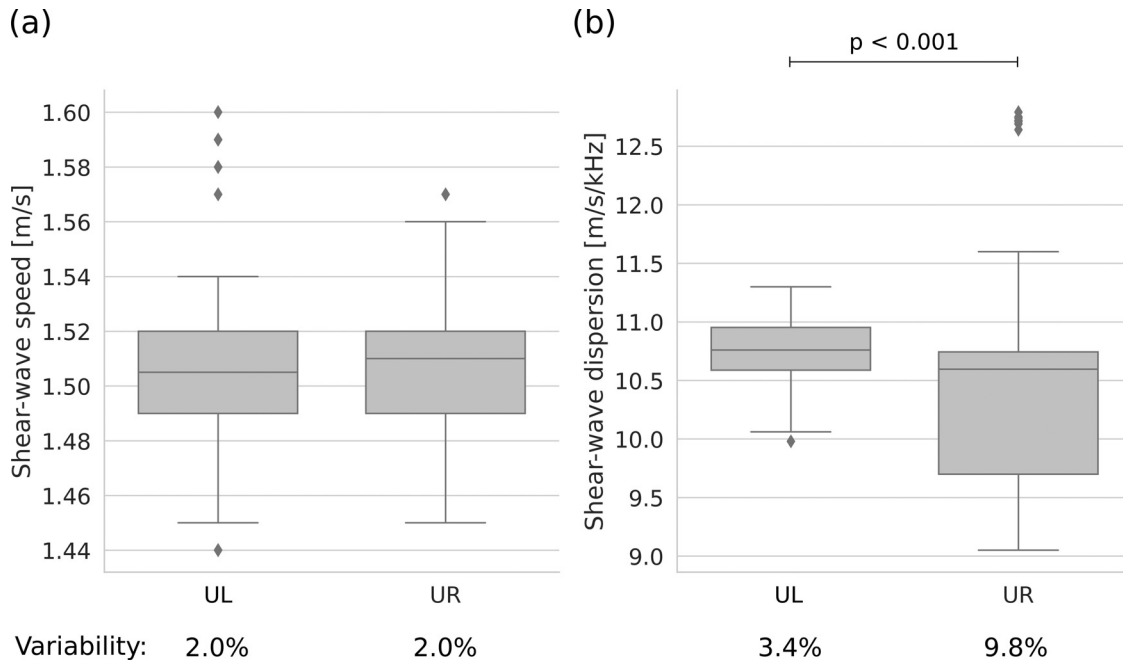


Fig. 10. Comparison of shear-wave speed (SWS) and shear-wave dispersion (SWD) values between region-of-interest locations in the upper left (UL) and upper right (UR) corners of the acquisition box and varying probe–phantom coupling conditions. A total of 100 measurements were acquired for each location. Variability is given by the ratio between the interquartile range and median. The p values indicate the statistical difference between medians. SWD exhibited higher variability than SWS. The UL location was more robust to inaccurate coupling conditions.

in the UR location were three times more variable than those in the UL location. Differences between the two positions were non-significant for SWS ($p = 0.78$) and significant for SWD ($p < 0.001$).

DISCUSSION

This study analyzed the effects of four different sources of variability in SWS and SWD measurements. The data were acquired using the Canon Aplio i800 US system in four homogeneous elasticity phantoms. The confounding variables studied included acquisition depth, lateral position and the size of the ROI, as well as size of the SWE acquisition box. Whereas such sources of variability have been extensively studied for SWS (Tozaki et al. 2011; Zhao et al. 2011; Chang et al. 2013; Hall et al. 2013; Wang et al. 2014; Carlsen et al. 2015; Shin et al. 2016; Rominger et al. 2018; Ruby et al. 2019), this work extended the analysis to SWD. The acquisition depth was the most important source of variability for both SWS and SWD. The lateral position of the ROI had effects on SWD with a magnitude similar to the acquisition depth. The overall variability caused by the size of the ROI and the acquisition box was not significant in both metrics.

Measured SWS values were lower than the certified values for all phantoms (Fig. 4a). This underestimation

was consistent with a previous study from our group (Ruby et al. 2019) that measured the same phantoms using the LOGIQ E9 US system (GE Healthcare). No certified values were available for SWD. Stiffer phantoms had higher SWD values (Fig. 4b) and, thus, higher viscosity. This relationship between elasticity and viscosity resembles the strong correlation between the two metrics in the liver (Chen et al. 2013). However, measured SWD values for the stiffest phantom were considerably larger than those typically observed in the liver. SWD values obtained using Canon Aplio systems are below 20 m/s/kHz (Lee et al. 2019; Sugimoto et al. 2020; Trout et al. 2020). Hence, analyzed confounding effects on SWD in the stiffest phantom may not be clinically relevant for the liver assessment.

In general, SWD measurements had two to three times higher variability than SWS measurements (Table 2). There are several reasons for this. First, SWS measures the group velocity of shear waves, whereas SWD relies on the estimation of phase velocity. The amount of energy in each frequency component is considerably smaller than the total energy of the signal that estimates SWS. Thus, phase velocity estimations are more vulnerable to errors caused by the lower signal-to-noise ratio (SNR). Furthermore, the energy of US signals is affected by frequency-dependent attenuation, which further decreases the SNR,

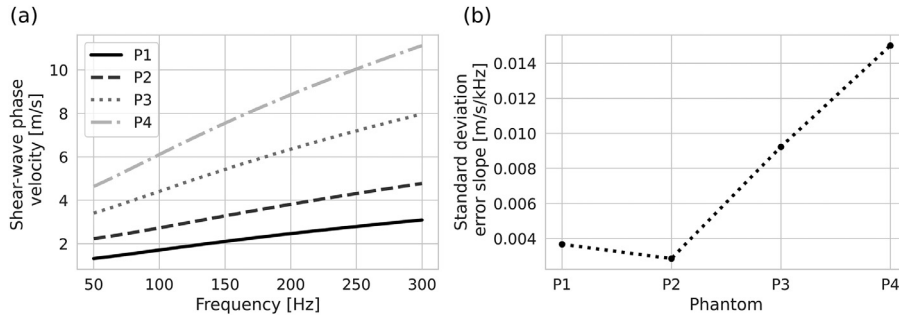


Fig. 11. (a) Shear-wave phase velocity dispersion curves predicted from the Voigt model for each phantom (P1–P4). We used the calibrated elasticity values of the phantoms and viscosity values that reproduce observed mean shear-wave dispersion (SWD) values in Table 2. Grid search was used to find viscosity values providing a dispersion curve slope that matches SWD measurements. (b) Standard deviation error of the slope obtained from linear regression analysis of (a). Larger slope errors indicate that curves in (a) deviate more from linear trends.

especially for higher-frequency components (Deffieux *et al.* 2009; Palmeri *et al.* 2021). If the variability in phase velocity estimations increases with frequency, the dispersion curve slope (SWD) may become very sensitive to noise-related errors.

Viscoelastic tissue properties are commonly described using the Voigt model (Catheline *et al.* 2004; Chen *et al.* 2009), which provides a non-linear relationship between phase velocities and frequencies. However, SWD estimations made in this study assume a linear relationship between these two quantities. This linear approximation is expected to be valid in the frequency range 50–300 kHz for typical viscoelastic properties of the liver (Barry *et al.* 2012; Nguyen *et al.* 2014; Nightingale *et al.* 2015). If the linear assumption is not satisfied, the estimations of the slope can exhibit high variability. Figure 11a illustrates the theoretical dispersion curves computed from the Voigt model using properties of the phantom that approximate our experimental observations of SWD. Figure 11b illustrates the standard deviation error of the slopes computed from linear regression. These errors are in general very small, and in principle, deviations from linearity appear negligible. Phantom P2 has the lowest errors and thus the strongest linear relationship. Interestingly, in our study, we also observed that P2 had the lowest variability (Table 2). The CoV of P2 was almost three times smaller than those of P1 and P3. This observation is important and may suggest that small deviations of dispersion curves from linear trends can substantially increase measurement variability. Thus, SWD values should be carefully interpreted when the linear assumption cannot be guaranteed.

This may be the case, for instance, in regions of the liver with a high blood vessel concentration.

The values of SWS were gradually underestimated with increasing acquisition depth (Fig. 7a). Several studies had reported similar depth-dependent biases in SWS (Tozaki *et al.* 2011; Zhao *et al.* 2011; Hall *et al.* 2013; Ewertsen *et al.* 2016; Shin *et al.* 2016; Ruby *et al.* 2019), attributing the decay to viscoelastic effects. Attenuation of US signals increases with increasing propagation distance and frequency. Attenuation therefore modifies the frequency spectrum of the acoustic radiation force used to generate shear waves. At deeper regions, lower frequencies will contribute more to the shear-wave group velocities (SWS). Because phase velocities increase with frequency in dispersive tissue (Chen *et al.* 2004), increasing the contribution of lower frequencies will reduce SWS values. Furthermore, if the dispersion curve slope (SWD) is increased, that is, if the relative difference in phase velocities between low and high frequencies becomes larger, SWS values will decay more with depth. This may explain why stiffer phantoms had a greater decrease in SWS compared with softer phantoms (Fig. 7a), similar to other studies (Carlsen *et al.* 2015). Convex US probes can also produce an apparent increase in SWS at shallow depths (<30 mm) (Zhao *et al.* 2011; Wang *et al.* 2014). Here, the focusing ability of the transducer in the elevational direction is suboptimal, and thus, the acoustic radiation force has an undesired size in the elevational plane, leading to a displacement of shear-wave sources from the lateral plane. As a consequence, SWS values are estimated considering a propagation path longer than the actual one.

When excluding the softest phantom, we found that SWD significantly decreased with acquisition depth ($p < 0.001$; see Fig. 7b). A decay in SWD can be caused only by frequency-dependent effects, that is, by effects that influence each phase velocity differently. As discussed, in viscoelastic media, attenuation depends on the frequency and lowers the SNR of higher-frequency components (Palmeri et al. 2021). This may affect the estimations of high-frequency phase velocities (Deffieux et al. 2009) and introduce biases in the computation of the dispersion slope. As phantom stiffness increases, the induced shear wave amplitudes decrease, and measurements become more difficult. Therefore, frequency-dependent noise-related errors are expected to be more significant in stiffer phantoms (Urban et al. 2009). Furthermore, as discussed, convex probes increase the values of SWS at shallow depths. If all phase velocities are multiplied by the same constant factor (which is > 1), then SWD will also experience an apparent increase at shallow regions.

In contrast, the softest phantom exhibited an increasing trend with depth ($p < 0.001$; see Fig. 7b). In soft tissue, the wavelength of the displacement field is large, especially at deeper regions in which higher-frequency components are attenuated more. If the tracking system does not correctly capture the complete displacement waveform, biases will be introduced in the SWD estimation, which relies on Fourier transform-based post-processing.

The lateral ROI position was an important variance-contributing factor for SWD (Fig. 5b). The CoV values were $> 20\%$ for P1, P3 and P4. Moreover, we found a significant systematic decrease in SWD when changing the ROI from the left to right position (Fig. 6b). In principle, we do not expect significant differences between these positions in a homogeneous medium unless there are asymmetries in our acquisition setup. We studied the origin of these variations by acquiring additional measurements with different coupling conditions between the US probe, gel and phantom. The results indicate that SWD measurements are more sensitive than SWS to the inadequate probe–phantom coupling (Fig. 10). Under this condition, US waves attenuate more rapidly, and as mentioned before, lower SNR affects phase velocity estimations in particular. Furthermore, we observed that the UR position had three times more variability than the UL position and is, therefore, more vulnerable to biases. The US system generates the first US radiation force close to the region where UL is located. Here, the wavefronts are nearly parallel, and they are gradually distorted during their propagation in the lateral direction (e.g., see Fig. 2a wavefront map). Because SWS and SWD estimations rely on the plane wave approximation, we expect measurements to be more robust in regions closer

to the first US radiation force (Fujii et al. 2019). Measurement locations that are too close to the excitation pulse could also lead to highly variable SWD values as a result of near-field effects (Kijanka et al. 2019). However, our results suggest that UL positions are nearly unaffected by such effects, which are minimized by the US system.

The variability caused by the sizes of the ROI and the SWE acquisition box was overall small and not significant. The ROI size controls the region in which local SWS and SWD values are averaged. In homogeneous media, larger ROI sizes perform better, with reduced SNR and variance (Deffieux et al. 2009), as illustrated in Figure 8. However, in clinical applications, increasing the ROI size becomes difficult because of tissue heterogeneities. We suggest avoiding very small ROI diameters (< 10 mm) to ensure reasonable measurement variability. Regarding the acquisition box, large dimensions increased the variability of both metrics and are not recommended (Fig. 9).

This study had several limitations. First, we assumed that the viscosity of the phantoms was homogeneous. However, the manufacturer did not provide certified values of their viscoelastic properties. The results of this study should therefore be validated in phantoms that are purpose built and certified for SWD analysis (Hall et al. 2013; Nguyen et al. 2014). Second, we interpreted SWD values without specific information on the shear-wave phase velocities. To better understand the confounding effects on SWD, we suggest comparing our results with those obtained with the magnetic resonance elastography technique (Urban et al. 2017). Last, the sources of variability considered here were limited by the parameters that the operator can modify in the US system. Other technical parameters controlling the characteristics of shear-wave excitation pulses could also affect SWS and SWD measurements. Moreover, this phantom study did not account for other sources of variability that arise in clinical applications. For example, the patient's age, fasting status, respiration or the examined hepatic lobe could influence SWE measurements (Goertz et al. 2012; Lee et al. 2013; Fontanilla et al. 2014; Jung et al. 2017).

CONCLUSIONS

This study presents a systematic analysis on operator-dependent confounding factors affecting SWD measurement variability. These effects are also compared with those influencing SWS values, which have been extensively studied in the literature. Compared with that of SWS, SWD variability was substantially larger and may limit its clinical use as a reliable biomarker. Multi-parametric elastography approaches, which complement

SWS measurements, may be better suited for this new metric. The acquisition depth and lateral position of the ROI were the most important variance-contributing factors for SWD, whereas only the acquisition depth was significant for SWS. Therefore, future guidelines and recommendations for multiparametric liver elastography should account for these two confounding variables.

Acknowledgments—The authors gratefully acknowledge Christoph Simm from Canon Medical Systems Europe for fruitful discussions and Bettina Baessler for advice in statistical analysis.

Conflict of interest disclosure—This work received financial support from Canon Medical.

REFERENCES

- Asrani SK, Devarbhavi H, Eaton J, Kamath PS. Burden of liver diseases in the world. *J Hepatol* 2019;70:151–171.
- Barry CT, Mills B, Hah Z, Mooney RA, Ryan CK, Rubens DJ, Parker KJ. Shear wave dispersion measures liver steatosis. *Ultrasound Med Biol* 2012;38:175–182.
- Bedossa P, Dargère D, Paradis V. Sampling variability of liver fibrosis in chronic hepatitis C. *Hepatology* 2003;38:1449–1457.
- Breiman L. Random forests. *Mach Learn* 2001;45:5–32.
- Carlsen JF, Pedersen MR, Ewertsen C, Sæftoiu A, Lönn L, Rafaelsen SR, Nielsen MB. A comparative study of strain and shear-wave elastography in an elasticity phantom. *Am J Roentgenol* 2015;204:W236–W242.
- Castera L. Noninvasive methods to assess liver disease in patients with hepatitis B or C. *Gastroenterology* 2012;142:1293–1302 .e4.
- Castera L, Yuen Chan HL, Arrese M, Afdhal N, Bedossa P, Friedrich-Rust M, Han KH, Pinzani MEASL-ALEH. Clinical Practice Guidelines: Non-invasive tests for evaluation of liver disease severity and prognosis. *J Hepatol* 2015;63:237–264.
- Catheline S, Gennisson JL, Delon G, Fink M, Sinkus R, Abouelkaram S, Culioli J. Measurement of viscoelastic properties of homogeneous soft solid using transient elastography: An inverse problem approach. *J Acoust Soc Am* 2004;116:3734–3741.
- Chang S, Kim MJ, Kim J, Lee MJ. Variability of shear wave velocity using different frequencies in acoustic radiation force impulse (ARFI) elastography: A phantom and normal liver study. *Ultraschall Med* 2013;34:260–265.
- Chen S, Fatemi M, Greenleaf JF. Quantifying elasticity and viscosity from measurement of shear wave speed dispersion. *J Acoust Soc Am* 2004;115:2781–2785.
- Chen S, Urban MW, Pislaru C, Kinnick R, Zheng Y, Yao A, Greenleaf JF. Shearwave dispersion ultrasound vibrometry (SDUV) for measuring tissue elasticity and viscosity. *IEEE Trans Ultrason Ferroelectr Freq Control* 2009;56:55–62.
- Chen S, Sanchez W, Callstrom MR, Gorman B, Lewis JT, Sanderson SO, Greenleaf JF, Xie H, Shi Y, Pashley M, Shamdasani V, Lachman M, Metz S. Assessment of liver viscoelasticity by using shear waves induced by ultrasound radiation force. *Radiology* 2013;266:964–970.
- Deffieux T, Montaldo G, Tanter M, Fink M. Shear wave spectroscopy for in vivo quantification of human soft tissues visco-elasticity. *IEEE Trans Med Imaging* 2009;28:313–322.
- Dhyani M, Xiang F, Li Q, Chen L, Li C, Bhan AK, Anthony B, Grajo JR, Samir AE. Ultrasound shear wave elastography: Variations of liver fibrosis assessment as a function of depth, force and distance from central axis of the transducer with a comparison of different systems. *Ultrasound Med Biol* 2018;44:2209.
- Ewertsen C, Carlsen JF, Christiansen IR, Jensen JA, Nielsen MB. Evaluation of healthy muscle tissue by strain and shear wave elastography - Dependency on depth and ROI position in relation to underlying bone. *Ultrasonics* 2016;71:127–133.
- Ferraioli G, Wong VWS, Castera L, Berzigotti A, Sporea I, Dietrich CF, Choi BI, Wilson SR, Kudo M, Barr RG. Liver ultrasound elastography: An update to the World Federation for Ultrasound in Medicine and Biology Guidelines and Recommendations. *Ultrasound Med Biol* 2018;44:2419–2440.
- Fontanilla T, Cañas T, Macía A, Alfageme M, Gutierrez Junquera C, Malalana A, Luz Cilleruelo M, Roman E, Miralles M. Normal values of liver shear wave velocity in healthy children assessed by acoustic radiation force impulse imaging using a convex probe and a linear probe. *Ultrasound Med Biol* 2014;40:470–477.
- Fujii S, Yamakawa M, Kondo K, Namita T, Shiina T. Evaluation of shear wave dispersion in hepatic viscoelastic models including fibrous structure. *Jpn J Appl Phys* 2019;58:SGGE07.
- Goertz RS, Egger C, Neurath MF, Strobel D. Impact of food intake, ultrasound transducer, breathing maneuvers and body position on acoustic radiation force impulse (ARFI) elastometry of the liver. *Ultraschall Med* 2012;33:380–385.
- Hall TJ, Milkowski A, Garra B, Carson P, Palmeri M, Nightingale K, Lynch T, Alturki A, Andre M, Audiere S, Bamber J, Barr R, Bercoff J, Bercoff J, Bernal M, Brum J, Chan HW, Chen S, Cohen-Bacrie C, Couade M, Daniels A, Dewall R, Dillman J, Ehman R, Franchi-Abella S, Fromageau J, Gennisson JL, Henry JP, Ivancevich N, Kalin J, Kohn S, Kugel J, Lee K, Liu N, Loupas T, Mazer-nik J, McAleavey S, Miette V, Metz S, Morel B, Nelson T, Nordberg E, Oudry J, Padwal M, Rouze N, Samir A, Sandrin L, Schaccitti J, Schmitt C, Shamdasani V, Song P, Switalski P, Wang M, Wear K, Xie H, Zhao H. RSNA/QIBA: Shear wave speed as a biomarker for liver fibrosis staging. *Proc IEEE Int Ultrason Symp* 2013;397–400.
- Jung C, Groth M, Petersen KU, Hammel A, Brinkert F, Grabhorn E, Weidemann SAW, Busch J, Adam G, Herrmann J. Hepatic shear wave elastography in children under free-breathing and breath-hold conditions. *Eur Radiol* 2017;27:5337–5343.
- Kijanka P, Ambrozinski L, Urban MW. Two point method for robust shear wave phase velocity dispersion estimation of viscoelastic materials. *Ultrasound Med Biol* 2019;45:2540–2553.
- Lee MJ, Kim MJ, Han KH, Yoon CS. Age-related changes in liver, kidney, and spleen stiffness in healthy children measured with acoustic radiation force impulse imaging. *Eur J Radiol* 2013;82:e290–e294.
- Lee DH, Lee JY, Bae JS, Yi NJ, Lee KW, Suh KS, Kim H, Lee KB, Han JK. Shear-wave dispersion slope from US shear-wave elastography: Detection of allograft damage after liver transplantation. *Radiology* 2019;293:327–333.
- Lee DH, Cho EJ, Bae JS, Lee JY, Yu SJ, Kim H, Lee KB, Han JK, Choi BI. Accuracy of two-dimensional shear wave elastography and attenuation imaging for evaluation of patients with nonalcoholic steatohepatitis. *Clin Gastroenterol Hepatol* 2021;19:797–805.
- Lipman SL, Rouze NC, Palmeri ML, Nightingale KR. Impact of acoustic radiation force excitation geometry on shear wave dispersion and attenuation estimates. *Ultrasound Med Biol* 2018;44:897–908.
- Nguyen MM, Zhou S, Robert J Luc, Shamdasani V, Xie H. Development of oil-in-gelatin phantoms for viscoelasticity measurement in ultrasound shear wave elastography. *Ultrasound Med Biol* 2014;40:168–176.
- Nightingale K, Rouze N, Rosenzweig S, Wang M, Abdelmalek M, Guy C, Palmeri M. Derivation and analysis of viscoelastic properties in human liver: Impact of frequency on fibrosis and steatosis staging. *IEEE Trans Ultrason Ferroelectr Freq Control* 2015;62:165–175.
- Ormachea J, Parker KJ. Comprehensive viscoelastic characterization of tissues and the inter-relationship of shear wave (group and phase) velocity, attenuation and dispersion. *Ultrasound Med Biol* 2020;46:3448–3459.
- Palmeri ML, Milkowski A, Barr R, Carson P, Couade M, Chen J, Chen S, Dhyani M, Ehman R, Garra B, Gee A, Guenette G, Hah Z, Lynch T, Macdonald M, Managuli R, Miette V, Nightingale KR, Obuchowski N, Rouze NC, Morris DC, Fielding S, Deng Y, Chan D, Choudhury K, Yang S, Samir AE, Shamdasani V, Urban M, Wear K, Xie H, Ozturk A, Qiang B, Song P, McAleavey S, Rosenzweig S, Wang M, Okamura Y, McLaughlin G, Chen Y, Napolitano D, Carlson L, Erpelding T, Hall TJ. Radiological Society of North America/Quantitative Imaging Biomarker Alliance shear wave speed bias quantification in elastic and viscoelastic phantoms. *J Ultrasound Med* 2021;40:569–581.

- Regev A, Berho M, Jeffers LJ, Milikowski C, Molina EG, Pyrsopoulos NT, Feng ZZ, Reddy KR, Schiff ER. Sampling error and intraobserver variation in liver biopsy in patients with chronic HCV infection. *Am J Gastroenterol* 2002;97:2614–2618.
- Rominger MB, Kälin P, Mastalerz M, Martini K, Klingmüller V, Sanabria S, Frauenfelder T. Influencing factors of 2D shear wave elastography of the muscle—An ex vivo animal study. *Ultrasound Int Open* 2018;4:E54–E60.
- Rousselet MC, Michalak S, Dupré F, Croué A, Bedossa P, Saint-André JP, Calès P. Sources of variability in histological scoring of chronic viral hepatitis. *Hepatology* 2005;41:257–264.
- Ruby L, Mutschler T, Martini K, Klingmüller V, Frauenfelder T, Rominger MB, Sanabria SJ. Which confounders have the largest impact in shear wave elastography of muscle and how can they be minimized? An elasticity phantom, ex vivo porcine muscle and volunteer study using a commercially available system. *Ultrasound Med Biol* 2019;45:2591–2611.
- Shiina T, Nightingale KR, Palmeri ML, Hall TJ, Bamber JC, Barr RG, Castera L, Choi BI, Chou YH, Cosgrove D, Dietrich CF, Ding H, Amy D, Farrokh A, Ferraioli G, Filice C, Friedrich-Rust M, Nakashima K, Schafer F, Sporea I, Suzuki S, Wilson S, Kudo M. WFUMB Guidelines and Recommendations for Clinical Use of Ultrasound Elastography: Part 1. Basic principles and terminology. *Ultrasound Med Biol* 2015;41:1126–1147.
- Shin HJ, Kim MJ, Kim HY, Roh YH, Lee MJ. Comparison of shear wave velocities on ultrasound elastography between different machines, transducers, and acquisition depths: A phantom study. *Eur Radiol* 2016;26:3361–3367.
- Sugimoto K, Moriyasu F, Oshiro H, Takeuchi H, Yoshimasu Y, Kasai Y, Furuichi Y, Itoi T. Viscoelasticity measurement in rat livers using shear-wave US elastography. *Ultrasound Med Biol* 2018;44:2018–2024.
- Sugimoto K, Moriyasu F, Oshiro H, Takeuchi H, Yoshimasu Y, Kasai Y, Itoi T. Clinical utilization of shear wave dispersion imaging in diffuse liver disease. *Ultrasonography* 2019;39:3–10.
- Sugimoto K, Moriyasu F, Oshiro H, Takeuchi H, Abe M, Yoshimasu Y, Kasai Y, Sakamaki K, Hara T, Itoi T. The role of multiparametric US of the liver for the evaluation of nonalcoholic steatohepatitis. *Radiology* 2020;296:532–540.
- Talwalkar JA, Kurtz DM, Schoenleber SJ, West CP, Montori VM. Ultrasound-based transient elastography for the detection of hepatic fibrosis: Systematic review and meta-analysis. *Clin Gastroenterol Hepatol* 2007;5:1214–1220.
- Tozaki M, Saito M, Joo C, Yamaguchi M, Isobe S, Ogawa Y, Homma K, Fukuma E. Ultrasonographic tissue quantification of the breast using acoustic radiation force impulse technology: Phantom study and clinical application. *Jpn J Radiol* 2011;29:598–603.
- Trout AT, Xanthakos SA, Bennett PS, Dillman JR. Liver shear wave speed and other quantitative ultrasound measures of liver parenchyma: Prospective evaluation in healthy children and adults. *Am J Roentgenol* 2020;214:557–565.
- Urban MW, Chen S, Greenleaf JF. Error in estimates of tissue material properties from shear wave dispersion ultrasound vibrometry. *IEEE Trans Ultrason Ferroelectr Freq Control* 2009;56:748–758.
- Urban MW, Chen J, Ehman RL. Comparison of shear velocity dispersion in viscoelastic phantoms measured by ultrasound-based shear wave elastography and magnetic resonance elastography. *Proc IEEE Int Ultrason Symp* 2017;1–4.
- Wang CZ, Zheng J, Huang ZP, Xiao Y, Song D, Zeng J, Zheng HR, Zheng RQ. Influence of measurement depth on the stiffness assessment of healthy liver with real-time shear wave elastography. *Ultrasound Med Biol* 2014;40:461–469.
- Wiegand J, Berg T. The etiology, diagnosis and prevention of liver cirrhosis. *Dtsch Arztebl Int* 2013;110:85–91.
- Zhao H, Song P, Urban MW, Kinnick RR, Yin M, Greenleaf JF, Chen S. Bias observed in time-of-flight shear wave speed measurements using radiation force of a focused ultrasound beam. *Ultrasound Med Biol* 2011;37:1884–1892.